Towards Terrain Adaptablity: In Situ Transformation of Wheel-Biped Robots

Tangyou Liu , Chao Zhang , Jiaole Wang , *Member, IEEE*, Shuang Song ,
and Max Q.-H. Meng , *Fellow, IEEE*

Abstract—Most existing bipedal robots can only move with either their wheels or feet. Even if some of them are capable of transforming between these two motions, they need to change their configuration dramatically. In order to truly combine the advantages of wheeled and footed robots, in this letter, an *in situ* transformation method is investigated and implemented on a wheel-biped transformable robot *SR600-II*. *In situ* transformation means a transforming process with minimum position and configuration changes. It includes two processes: foot-to-wheel (FtW) and wheel-to-foot (WtF) transformations, both of which have to pass by transition states (termed critical states) that both foot and wheel contact with floor. At critical states, the robot has to meet both constraints of wheeled and footed balances. For footed balance, the center of mass (CoM) needs to fall within the support polygon formed by the feet. In order to maintain *in situ* wheeled balance, the upper body posture needs to be adjusted in real-time during the transformation process to make the vertical projection of the CoM be kept between the two wheels. To achieve a smooth transformation and minimize changes in robot joints, a projection-based algorithm is proposed to adjust the robot posture to comply with both constraints. Simulations and experiments on the *SR600-II* prototype have validated the effectiveness of the proposed design and control strategy for wheel-biped transformable robots.

Index Terms—Wheel-biped robot, multi-motion, wheel-biped *in situ* transform.

I. INTRODUCTION

ADAPTABILITY and efficiency have always been the research focus of mobile robots. To promote adaptability, many researches have been focused on legged robots, such as quadrupedal and bipedal robots. Hutter *et al.* [1] developed a quadrupedal robot towards harsh environments, and [2] from Boston Dynamics presented a compact, nimble four-legged robot that can trot around office, home or outdoors. Bipedal robots [3]–[5] also showed excellent adaptability in door or outdoor. To boost efficiency, although there are a lot of researches on actuators such as [6], the most direct and effective way is to use wheels on a smooth floor. In [7]–[10] two wheeled platform were used to get higher efficiency and operating mobility. Although the robots mentioned above achieved satisfactory results in their own fields, there are increasing requirements for robots to have both adaptability and efficiency simultaneously.

Wheel-legged systems offer a promising solution to combine the advantages of wheeled and bipedal robots. In general, current wheel-legged robotic systems can be divided into two categories: wheel-quadruped and wheel-biped robots. *Momaro* [11] and *ANYmal* [12] were two representative wheel-quadruped robots which can drive with wheels and overcome obstacles by legs. Kashiri *et al.* [13] developed a wheel-quadruped mobile manipulator *Centauro*. Peng *et al.* [14] proposed a wheel-leg mobile robot using four Stewart platform as its legs. Bouton *et al.* [15] developed a compliant wheel-on-leg mobile robot that conforms to uneven terrain. Chen *et al.* [16] investigated a roller-skating quadrupedal robot with passive wheels. They showed that the roller-skating gait has higher speed and efficiency than the trotting gait.

Besides the aforementioned wheel-quadruped robots, wheel-biped robots have shown some special functionalities. Boston Dynamics developed a wheel-biped robot *Handle* which can jump, hold loads and run in outdoor scenarios [17]. Klemm *et al.* [18] presented a wheel-biped robot *Ascento* which applied LQR-assisted whole-body control strategy to stabilize the non-minimum phase dynamics of the wheel-biped robot. With a similar structure to *Handle*, [19] presented a hydraulic wheel-biped robot *WLR*. Chen *et al.* [20] studied jumping for wheeled-bipedal robots. It is noted that the aforementioned researches on wheel-legged robots have not focused on wheel-foot transformation. If *in situ* wheel-foot transformation can be achieved, then the advantages of legs and wheels will be further amplified, especially for biped robots.

Based on parallel mechanism, Hashimoto *et al.* [21] designed a wheel-biped robot *WL-16* which can realize walking and wheel-driven locomotion. Lim *et al.* [22] presented a wheeled humanoid robot *DRC-HUBO+* which can transform between walking and driving modes. In the driving mode, legs were only used for supporting, the robot was in a crouched position with a fixed height. Until now no biped robot can achieve *in situ* transformation between wheeled and footed motions without compromising the advantages of legs.

In this paper, a wheel-biped *in situ* transformation method is designed. The wheel-biped *in situ* transformation includes two parts: foot-to-wheel (FtW) transform and wheel-to-foot (WtF)
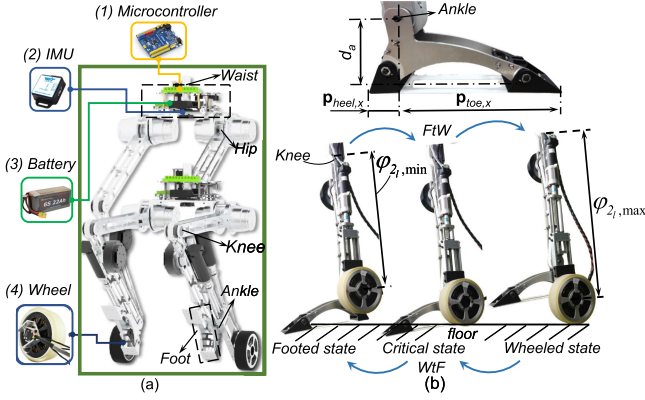
Fig. 1. The wheel-biped transformable robot *SR600-II*. (a) Components include: (1) Microcontroller controls the robot at 200 Hz; (2) IMU estimates the robot's torso posture, angular rate, and linear acceleration; (3) The robot is powered by two three-cell lithium-polymer batteries in series; (4) Wheel is driven by the motor directly to minimize backlash. (b) The transformation process, in which the wheel can be stretched out and retracted by a lead screw module driven by motor. The inlet shows the definition of d_a, $\mathbf{p}_{heel,x}$ and $\mathbf{p}_{toe,x}$ used in the following sections.

transform. To verify the proposed method, a transformable robot *SR600-II* is also presented, shown in Fig. 1, by redesigning the wheel-biped robot in our previous work [23]–[25]. This transformable robot is expected to move with either wheels or feet and perform wheel-biped *in situ* transformation. A lumped inverted pendulum (LIP) model and a linear quadratic regulator (LQR) controller are introduced to enable *SR600-II* to maintain dynamic wheeled balance. The control strategy, which includes a projection-based algorithm and a CoM-constrained inverse kinematic model, has been proposed to minimize the displacement of the center of mass (CoM) while performing the transformation (termed *in situ* transformation).

The remainder of paper is organized as follows: Section II develops kinematic and dynamic model for the transformable robot. It also presents balance constraints for both the footed and wheeled motions. The proposed projection-based algorithm and stability controller is investigated in Section III. The transformation strategy is verified by systematical simulations and experiments on a prototype in Section IV. Finally, we draw some conclusions and discuss about the future work in Section V.

II. MODELING

A. Coordinates & Assumptions

Because this paper focuses on solving the *in situ* transformation problem on a flat floor, identical motions are considered on both right and left legs during the locomotion and the transformation processes. In order to model and estimate the states of the system, we introduce a set of variables shown in Fig. 2. frame {0} is established as a reference for the upper-body at the midpoint between two wheels. frame {6} is fixed on the waist link to estimate its pose. θ denotes the tilt angle of the robot; v is the planar linear velocity; L indicates the distance from frame {0} to CoM; h is the distance from hip axis to wheel axis. To characterize mobility, we use x, y and γ to denote planar coordinates for position and orientation and d_t as the traveled trajectory length during transformation. $\varphi_{\{i_r, i_l\}}$ denotes the corresponding joint angle on the i-th joint on right (r) and left (l) sides. And τ_w is the torque generated by wheel motor.
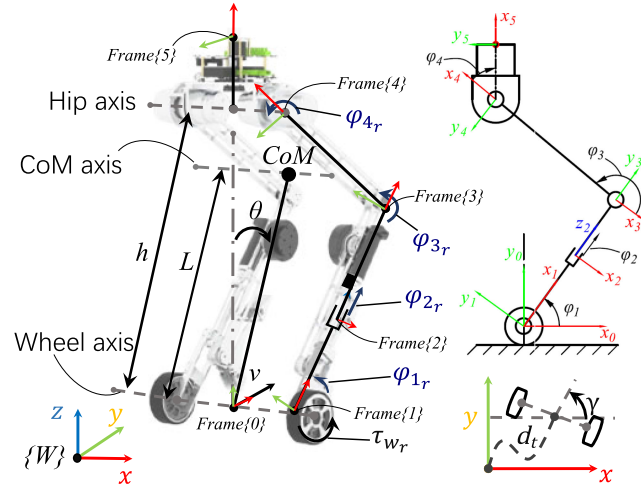

Fig. 2. Modeling of *SR600-II*, in a diagonal view (left), a right view (upper right) and top view (lower right).

Because right and left legs have identical motions, we only use variables on the right side for brevity hereon. Here, the joint angles and actuation torques are marked on the right leg only.

B. Kinematic & Dynamic Modeling

As shown in [23], Denavit-Hartenberg (D-H) convention was used to establish the kinematic model and to derive the CoM-based constraint for *in situ* transformation. Generally, the wheeled motion can be reduced to a two-wheeled LIP model of a specific height.

1) CoM-Constrained Kinematics: After transforming the CoM positions of each link to frame {0}, the CoM position of the robot ($^0\mathbf{p}_C$) can be obtained as

$$^0\mathbf{p}_C = \frac{\sum_{i=1}^n \left(^0\mathbf{p}_{O_i} + {}^0_i\mathbf{R}\,{}^i\mathbf{p}_{C_i} \right) M_i}{\sum_{i=1}^n M_i}, \quad (1)$$

where M_i is the mass of i-th link, $^0\mathbf{p}_{O_i}$ is the origin position of frame {i} in frame {0}, $^0_i\mathbf{R}$ denotes the rotation matrix from frame {i} to frame {0}, and $^i\mathbf{p}_{C_i}$ is the CoM position vector of the i-th link in frame {i}.

In order to achieve the wheeled balance, the vertical projection of CoM must be kept between two wheels. Therefore, we constrained the x coordinate of the CoM position $^0\mathbf{p}_{C,x} = 0$. We also constrained frame {6} to be aligned with frame {0}. Based on the relationship between h and φ_{i_r}, we can get the CoM-constrained kinematic model as

$$\begin{cases} h = L_t \cos \varphi_{4_r} + \varphi_{2_r} \sin \varphi_{1_r} \\ \varphi_{4_r} = -\arcsin \frac{A \cos \varphi_{1_r}}{B} \\ \varphi_{3_r} = \pi - \varphi_{1_r} - \varphi_{4_r} \end{cases}, \quad (2)$$

where L_t is the length of thigh link, and A, B are intermediate variables defined as follows:

$$A = (2M_3 + M_4)\,\varphi_{2_r} + 2M_1{}^1\mathbf{p}_{C_{1,x}} + 2\left(\varphi_{2_r} - {}^3\mathbf{p}_{C_{2,x}} \right) M_2,$$

$$B = 2M_3{}^3\mathbf{p}_{C_{3,x}} + M_4 L_t.$$

It can be seen from (2) that h is related to φ_{1_r}, φ_{2_r} and φ_{4_r} at the same time. Given some h, the remaining φ_{i_r} can be calculated for different φ_{2_r}.
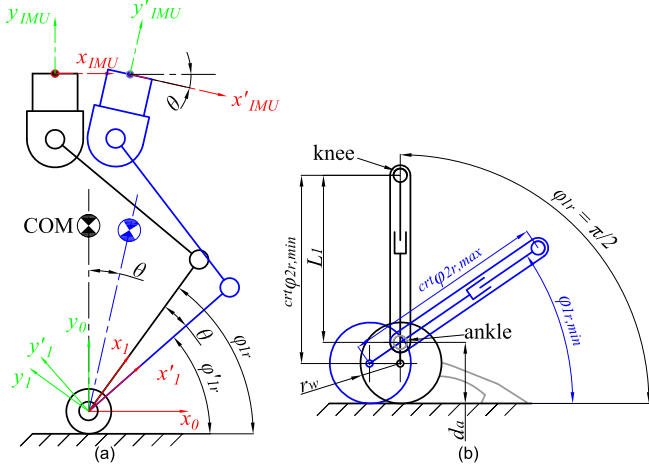
Fig. 3. (a) The relationship of IMU pitch angle, forward tilt angle θ and $\varphi_{\{1_r, 1_l\}}$. The dark black line represents the target posture of the system, and the blue line represents its current posture. (b) The maximum and minimum $^{crt}\varphi_{2_r}$ for the deepest squat (blue) and upright pose (black), where the foot is plotted in gray. In this study, the minimum and maximum values of φ_1 are 45° and 90°, and of $^{crt}\varphi_2$ are 460 mm and 530 mm, respectively.

Fig. 4. Constraints of footed balance. (a) Joint space of the right leg (φ_{1_r}, φ_{3_r}), the left leg is identical. The black dot lines indicate the joint limitations, and the magenta curves are the corresponding relationship curves of (φ_{1_r}, φ_{3_r}) for different $^{crt}\varphi_{2_r}$ in wheeled balance. The red arrow shows the increase direction of the critical φ_{2_r}. (b) Corresponding Cartesian space of CoM (red dots) and hip joint (black pentagrams). The black dot lines indicate the limitations of the footed support polygon.

The posture of the robot in wheeled balance is defined by φ_{i_r} where $i \in \{1, 2, 3, 4\}$. φ_{1_r} will be adjusted by the LQR controller automatically. In Fig. 3(a) we show that when the posture is locked, the forward tilt angle θ of CoM is equal to the error between current φ'_{1_r} and targeted φ_{1_r}. It is also equal to the pitch angle measured by the IMU on the waist link.

2) Dynamics of LIP: The dynamics of the lumped system in wheeled motion can be formulated as

$$\mathbf{M}(\mathbf{q})\ddot{\mathbf{q}} + \mathbf{V}(\mathbf{q}, \dot{\mathbf{q}}) + \mathbf{G}(\mathbf{q}) = \mathbf{S}^{\mathrm{T}}\mathbf{m}, \qquad (3)$$

where $\mathbf{q} = [\theta \, s \, \gamma]^{\mathrm{T}}$, $\mathbf{M}(\mathbf{q}) \in \mathbb{R}^{n_u \times n_u}$ donates the mass matrix and will be calculated for each posture, $\mathbf{V}(\mathbf{q}, \dot{\mathbf{q}}) \in \mathbb{R}^{n_u}$ donates the vector of Coriolis and centrifugal terms, and $\mathbf{G}(\mathbf{q}) \in \mathbb{R}^{n_u}$ is the vector of gravity terms. The selection matrix $\mathbf{S}(\mathbf{q}) \in \mathbb{R}^{n_u \times n_u}$ selects the acting actuation torques $\mathbf{m}$. $n_u = 6$ in this study. All parameters needed in the calculation are determined from precise measurements of all used components and calculated by computer-aided design models.

C. Balance Constraints

1) Critical State: In order to explore the control strategy of WtF and FtW transformations, we need to analyze the constraints of the two balance states. More importantly, we need to investigate the transition process from one balance state to another. During the transition process, there are a serial of critical states that both wheels and feet are contacting the floor. As shown in Fig. 3(b), these critical states can be formed by varying the robot posture while maintaining the aforementioned contact.

To visually show the relationship between the robot posture and the critical φ_{2_r} ($^{crt}\varphi_{2_r}$), Fig. 3(b) shows the diagrams of wheel and foot in two critical states when the upper body is at the deepest ($^{crt}\varphi_{2_r, max} = mm$) and upright ($^{crt}\varphi_{2_r, min} = 475 \, mm$) postures. This geometric relationship can be defined as

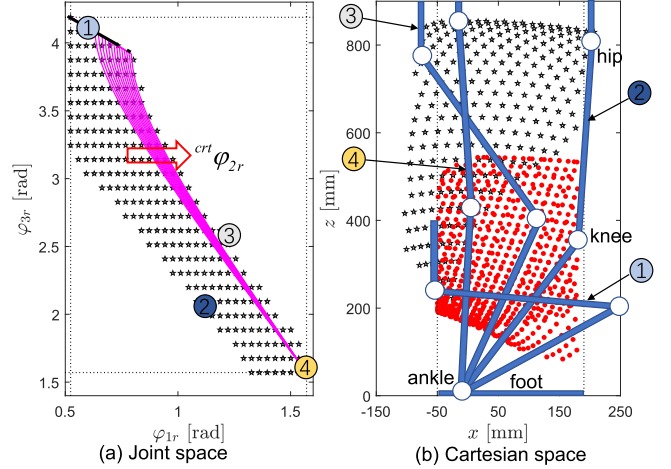$$^{crt}\varphi_{2_r} = \frac{d_a - r_w}{\sin \varphi_{1_r}} + L_1, \qquad (4)$$

where L_1 is the distance from knee to ankle joint, r_w is the radius of wheel, d_a is the distance from ankle joint to floor. In Fig. 3(b), $\varphi_{1_r, min}$ denotes the minimum value of φ_{1_r} which corresponds to $^{crt}\varphi_{2_r, max}$ and the deepest posture of the robot.

2) Constraints of Footed Balance: When the robot maintains balance with two feet, it is necessary to make CoM position meet the zero moment point (ZMP) principle [26] as follows,

$$\mathbf{p}_{heel,x} \leq \mathbf{p}_{C_x} \leq \mathbf{p}_{toe,x}, \qquad (5)$$

where $\mathbf{p}_{C_x}$, $\mathbf{p}_{heel,x}$ and $\mathbf{p}_{toe,x}$ are the x coordinates of CoM, heel and toe positions. Here, this inequality constraint was used to analyze the constraints in joint and Cartesian spaces of *SR600-II* in the footed state by mimicking human squatting [27].

During the footed squat, the calf length φ_{2_r} can be set to any value in the range between the minimum ($\varphi_{2_r, min}$) and the critical value of current posture ($^{crt}\varphi_{2_r}$), inside which the feet contact with the floor and the posture does not vary with it. Because frame {6} is aligned with frame {0}, only φ_{1_r} and φ_{3_r} are independent variables. By sampling these two joints uniformly inside their ranges and applying the above inequality constraint, we can firstly obtain the balanced joint space by eliminating the unbalanced postures as shown in Fig. 4(a). Then, the corresponding balanced Cartesian spaces of the hip joint and CoM are shown in Fig. 4(b).

In Fig. 4, four representative postures are used to further explain the mapping between joint and Cartesian spaces:

- The deepest straight down squat posture. The ankle joint reaches the minimum limit;
- A forward posture. The CoM is close to the front edge of the toe;
- A backward posture. The CoM is close to the rear edge of the heel;
- The straight leg posture. Because the floor projection of CoM is on the ankle axis, the knee joint is slightly bent and the hip joint is slightly leaned towards heel.

3) Constraints of Wheeled Balance: During the *in situ* wheel-biped transformation process, when φ_{2_r} exceeds the
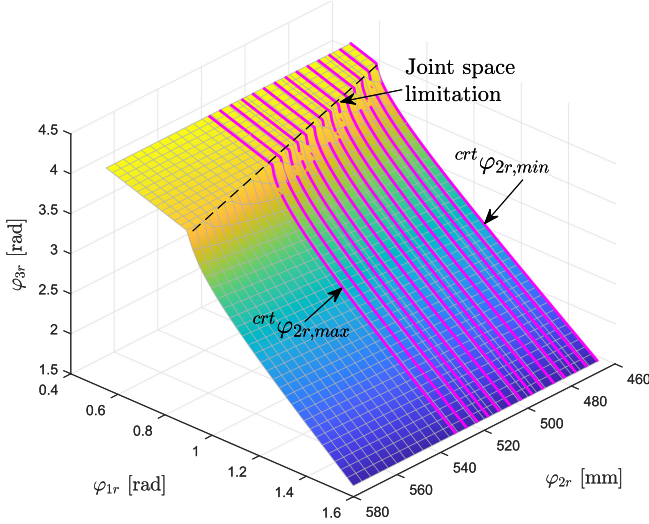
Fig. 5.   Constraints of wheeled balance in joint space. The dashed line is limitation of the joint space, above which the data points are unreachable solutions. $^{crt}\varphi_{2_r,max}$ and $^{crt}\varphi_{2_r,min}$ denote the maximum and minimum critical φ_{2_r} values, respectively.

$^{crt}\varphi_{2_r}$ of current posture, feet will not contact with floor according to (4). The robot will have to use two wheels to maintain balance. When the robot maintains wheeled balance, (2) has constrained the vertical projection of CoM onto the wheel axis. From (2) we can further get the relationship between φ_{1_r}, φ_{2_r} and φ_{3_r} as

$$\varphi_{3_r} = \pi - \varphi_{1_r} + \arcsin \frac{(D\varphi_{2_r} + E)\cos\varphi_{1_r}}{B}, \quad (6)$$

where

$$D = 2\left(M_2 + M_3\right) + M_4,$$
$$E = 2\left(^1\mathbf{p}_{C_{1,x}}M_1 - {}^3\mathbf{p}_{C_{2,x}}M_2\right).$$

By sampling φ_{1_r} and φ_{2_r} uniformly in their ranges, we can solve the corresponding φ_{3_r} using (6). Then, the constraint surface can be plotted using these data points as shown in Fig. 5. The magenta curves in Fig. 5 show different slices of the surface at different $^{crt}\varphi_{2_r}$ values in wheeled balance. All critical states can be represented using all $^{crt}\varphi_{2_r}$ values within the range $[^{crt}\varphi_{2_r,min}, {}^{crt}\varphi_{2_r,max}]$.

4) Constraints of Critical State: At a critical state, the robot is at footed and wheeled balance states simultaneously. Of note, the black dots in Fig. 4(a) and magenta curves in Fig. 5 have already shown the constraints of footed and wheeled balances at critical state, respectively. Therefore, we can obtain the constraints of critical state by super-imposing them together in Fig. 4(a). It is clear that, at all critical states, the footed constraints include the wheeled constraints.

When the robot performs WtF transformation by retracting its wheels through the transformation module (reducing φ_{2_r}), it will always meets both wheeled and footed balance constraints. When it performs FtW transformation by extending its wheels (increasing φ_{2_r}), however, balance constraints will become more stringent. In FtW transformation, the robot needs to reconfigure its joints to meet the wheeled constraints at critical states (shown as the magenta curves).

Algorithm 1: Projection-based FtW Transformation Algorithm.

Input: $^0\mathbf{s} = [^0\varphi_{1_r}, {}^0\varphi_{3_r}]^T$, $k = 0$
Output: $^*\mathbf{s} = [^*\varphi_{1_r}, {}^*\varphi_{3_r}]$
  while $||\Delta\mathbf{s}||^2 > e$ **do**
    Solve $^{k+1,crt}\varphi_{2_r}$ using (9);
    while $||^{k+1}\mathbf{s}_i - {}^k\mathbf{s}|| - ||^{prj}\mathbf{s}_i - {}^k\mathbf{s}|| > e$ **do**
      Solve $^{k+1}m(^{k+1}\varphi_{1_r,i})$ using (10);
      Find tangent line by substituting $^{k+1}\mathbf{s}_i$ to (13);
      Solve $^{prj}\mathbf{s}_i$ by (14) and (15);
      Solve $^{k+1}\mathbf{s}_{i+1}$ by substituting $^{prj}\varphi_{1_r,i}$ to (10);
      i++;
    end while
    $^{k+1}\mathbf{s} = {}^{prj}\mathbf{s}_i$;
    $||\Delta\mathbf{s}|| = ||^{k+1}\mathbf{s} - {}^k\mathbf{s}||$;
    k++;
  end while
  return $\mathbf{s}^* = {}^k\mathbf{s}$;

III. IN SITU TRANSFORMATION ALGORITHM & CONTROL

It is non-trivial to simultaneously maintain footed and wheeled balances in the critical state during the *in situ* FtW transformation. When the transformation starts from a footed balanced posture but not complied with the constraint of wheeled balance, such as a black point that is not on the magenta curves as shown in Fig. 4(a), simply extending the wheels will results in a failure. To achieve a smooth FtW transformation, an algorithm should be introduced to adjust the robot posture to comply with both constraints.

The rationale of the *in situ* transformation algorithm is to minimize the changes in robot joints by an iterative approach. We first define an arbitrary point in Fig. 4(a) as $\mathbf{s} = [\varphi_{1_r}, \varphi_{3_r}]^T$. In every iteration, we need to find an optimal point ($^*\mathbf{s} = [^*\varphi_{1_r}, {}^*\varphi_{3_r}]^T$) that minimize the joint changes. The proposed algorithm can find a series of optimal points that minimize the joint changes for each iteration. Then, the target point can be obtained from the last iteration.

With out loss of generality, the optimization problem in the $(k+1)$-th iteration is defined as

$$^{k+1}\mathbf{s} = \arg\min_{\mathbf{s}} ||\mathbf{s} - {}^k\mathbf{s}||^2, \quad (7)$$

$$\text{s.t. } ^{k+1}f(\mathbf{s}) = 0, \quad (8)$$

where $^{k+1}f(\mathbf{s})$ is the constraint of critical states for the wheeled balance in the $(k+1)$-th iteration, i.e., one of the magenta curves in Fig. 4(a).

Because each critical state corresponds to a $^{crt}\varphi_{2_r}$, by submitting $^k\varphi_{1_r}$ of the k-th iteration to (4) we can get $^{k+1,crt}\varphi_{2_r}$ of the $(k+1)$-th iteration as

$$^{k+1,crt}\varphi_{2_r} = \frac{d_a - r_w}{\sin {}^k\varphi_{1_r}} + L_1. \quad (9)$$

Next, submitting $^{k+1,crt}\varphi_{2_r}$ to (2), we can finally find the constraint of critical states for the wheeled balance as

$$^{k+1}f(\mathbf{s}) = \varphi_{3_r} + \varphi_{1_r} - \arcsin \frac{^{k+1}A\cos\varphi_{1_r}}{^{k+1}B} - \pi = 0. \quad (10)$$
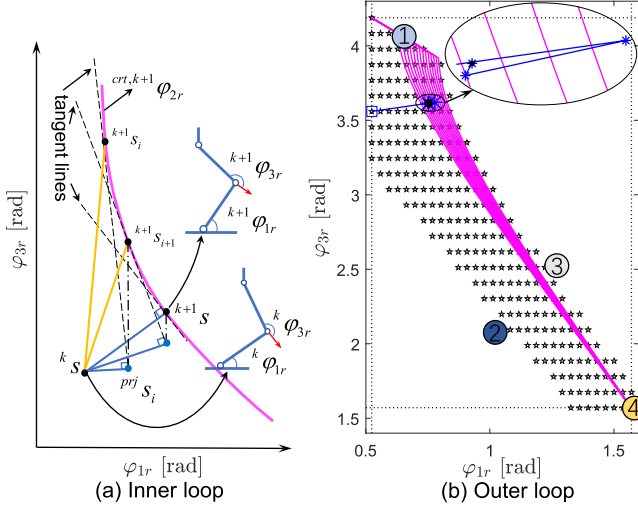
Fig. 6. The iteration process of Algorithm 1. (a) The diagram of inner loop. The magenta curve is the corresponding relationship curve of $(\varphi_{1_r}, \varphi_{3_r})$ for $^{crt,k+1}\varphi_{2_r}$ in wheeled balance. The two inlets represents the postures in $^k s$ and ^{k+1}s respectively. The black dashed lines are the corresponding tangent lines for different iterative steps. The yellow lines and blue lines indicate the distance from $^k s$ to tangent points and perpendicular projection points, respectively. (b) The iterative process of outer loop. Point marked with a blue square represent joints position before the FtW transformation. The blue line, connecting the two points marked with asterisk, is the iteration path, and the partially enlarged view shows the iterative process. The point marked with the black dot is the nearest point calculated by the Algorithm 1.

There are several methods to solve the aforementioned optimization problem, such as iterative search and geometry-based methods. After careful geometrical analysis, we can reformulate this problem to find a point on the magenta curve that minimizes the distance from the point of previous iteration (^{k}s). The nearest joints $^{k+1}\mathbf{s} = [^{k+1}\varphi_{1_r}, ^{k+1}\varphi_{3_r}]^T$ can be found from the following system of non-linear equations

$$ ^{k+1}m \left(^{k+1}\varphi_{1_r} \right) \frac{^{k+1}\varphi_{3_r} - {}^k\varphi_{3_r}}{^{k+1}\varphi_{1_r} - {}^k\varphi_{1_r}} = -1, \qquad (11) $$

$$ ^{k+1}f \left(^{k+1}\mathbf{s} \right) = 0. \qquad (12) $$

where $^{k+1}m(\varphi_{1_r}) = \frac{d\varphi_{3_r}}{d\varphi_{1_r}}$ is the slope function of curve defined by (10), and $^{k+1}m(^{k+1}\varphi_{1_r})$ is the slope at $^{k+1}$s. Then, update $k \leftarrow k+1$ and continue to solve the aforementioned optimization problem until the convergence criterion $\|^{k+1}\mathbf{s} - {}^k\mathbf{s}\|^2 \le e$ has met. Here, e is a pre-defined threshold and it is set to 0.01 in our implementation. Thus, we can find the target $\mathbf{s}^* = {}^{k+1}\mathbf{s}$.

To solve the system of non-linear equations (11), (12), we used a projection-based iterative method shown in Fig. 6(a). At the i-th iteration, we start at point $^{k+1}\mathbf{s}_i = [^{k+1}\varphi_{1_r,i}, ^{k+1}\varphi_{3_r,i}]^T$ and obtain the tangent line function of the corresponding critical curve at that point as

$$ \varphi_{3_r} = {}^{k+1}m(^{k+1}\varphi_{1_r,i})(\varphi_{1_r} - {}^{k+1}\varphi_{1_r,i}) + {}^{k+1}\varphi_{3_r,i}. \quad (13) $$

Then, we can get the perpendicular projection $^{prj}\mathbf{s}_i = [^{prj}\varphi_{1_r,i}, ^{prj}\varphi_{3_r,i}]^T$ of ^{k}s onto this tangent line by solving

	Part	Length (m)	Mass (kg)
	Thigh (L_t)	0.410	1.532
SR600-II	Calf [1] ($\varphi_{\{2_r,2_l\}}$)	0.438~0.568	1.956 (1.411)
	Foot[2] ($\mathbf{p}_{heel,x} + \mathbf{p}_{toe,x}$)	0.024	0.269 (0.1814)

[1] The mass is the mass of calf and wheel (or calf and foot).
[2] The mass is the mass of foot (or wheel).

$$ ^{prj}\varphi_{1_r,i} = \frac{(^{k+1}\varphi_{1_r,i} + {}^k\varphi_{1_r})^{k+1}m(^{k+1}\varphi_{1_r,i}) + {}^k\varphi_{3_r} - {}^{k+1}\varphi_{3_r,i}}{1/^{k+1}m(^{k+1}\varphi_{1_r,i}) + {}^{k+1}m(^{k+1}\varphi_{1_r,i})}, \quad (14) $$

$$ ^{prj}\varphi_{3_r,i} = \frac{-1}{^{k+1}m(^{k+1}\varphi_{1_r,i})(^{prj}\varphi_{1_r,i} - {}^k\varphi_{1_r})} + {}^k\varphi_{3_r}. \quad (15) $$

This inner iteration loop will stop if the convergence criterion $\|^{k+1}\mathbf{s}_i - {}^k\mathbf{s}\|^2 - \|^{prj}\mathbf{s}_i - {}^k\mathbf{s}\|^2 \le e$ has met, then we can get the $^{k+1}\mathbf{s} = {}^{prj}\mathbf{s}_i$. Otherwise, submitting the $^{prj}\varphi_{1_r,i}$ in (10), we can get the start point for $(i+1)$-th iteration. The corresponding algorithm is shown in Algorithm 1.

A diagram of the inner iteration loop in Algorithm 1 is shown in Fig. 6(a), in which $^{k+1}\mathbf{s}$ has been found in three iterations. In Fig. 6(b), it costs about four iterations of the outer loop to find the $^*\mathbf{s}$ using the proposed algorithm and the total computing time is 0.248 s using a non-optimized MATLAB code on a laptop with i7-10510 U CPU and 32 G RAM. After obtaining the targeted posture in footed balance, the FtW transformation can be performed through extending the transformation module (increase the φ_{2_r}). When $\varphi_{2_r} = {}^{crt}\varphi_{2_r}$ there will be a rapid current decrease of ankle motors, because the supporting force on feet has been shared by wheels. After detecting the rapid current decrease of ankle motor, the LQR controller will be enabled to maintain wheeled balance. Then, the robot will continue extending φ_{2_r} to $\varphi_{2_r,max}$ and adjusting its posture to meet the CoM constraint (2), until FtW transformation is finished.

WtF transformation is much more straight-forward than the FtW one. According to Fig. 4, the joint space of footed balance includes the critical joint space of wheeled balance. When the robot transformations from the wheeled balance to footed balance by decreasing φ_{2_r} from $\varphi_{2_r,max}$ to the critical value $^{crt}\varphi_{2_r}$, it needs to coordinate the knee and ankle joints to meet the CoM constraint (2). To ensure the *in situ* transformation, the LQR controller should be turned off after detecting the rapid current increase of ankle motor. Then, the robot will be in the footed balance state when it continue retracting φ_{2_r} to $\varphi_{2_r,min}$, until the WtF transformation is finished.

IV. SIMULATIONS & EXPERIMENTS

A. Simulations

In order to verify the algorithm and control method proposed in Section III, we carried out simulations using a simplified model with the parameters as shown in Table I. The simulation of FtW transformation was presented as a continuous process, in which the robot squatted from the upright initial state to the lowest point in footed balance, and finally transformed to wheeled balance. The corresponding data of IMU installed on the waist link is shown in Fig. 7-FtW phase. The WtF transformation was presented as a reverse of FtW transformation through another process. The corresponding data are shown in Fig. 7-WtF phase.
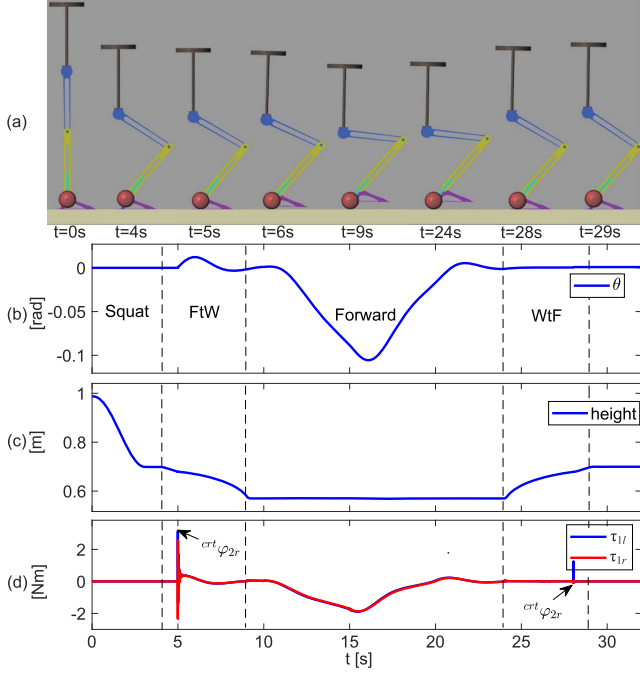
Fig. 7.   The simulation results of FtW & WtF transformations. In plot (b), init phase means the squat action, FtW (WtF) phase is the in *situ* transformation process of footed (wheeled) to wheeled (footed) balance, and forward phase indicates the forward moment.
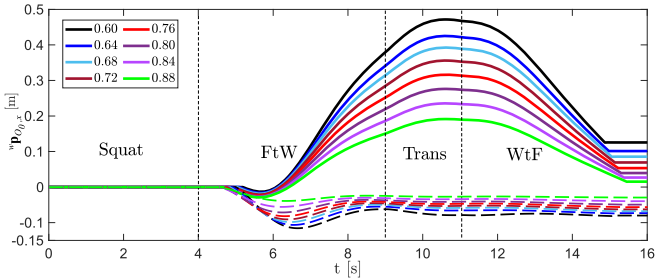

Fig. 8.   Comparison of $^{w}\mathbf{p}_{O_0,x}$ for different h in simulations with and without the proposed algorithm. The dashed and solid curves denote the simulations with and without the proposed algorithm, respectively.

According to the results, it is clear that the proposed strategy can be applied on the system to make it transform *in situ* successfully.

To further analyze the performance of *in situ* transformation, a series of simulations with and without proposed algorithm have been carried out in different configurations (corresponding to different h). The results are shown in Fig. 8 and 9. The robot squatted to different postures during 0~4 s. Then it performed the FtW and WtF transformations in FtW phase (4~9 s) and WtF phase (11~16 s), respectively. The Trans phase (9~11 s) was a transient period for recovering between different actions.

As shown in Fig. 8, the x coordinate of origin position of frame $\{0\}$ in frame $\{W\}$, $^{w}\mathbf{p}_{O_0,x}$ increases (decreases) greatly when it performs the FtW (WtF) transformation without the proposed algorithm. This is because when the robot extends (retracts) its wheels without posture adjustment, the robot will have a large forward (backward) inclination disturbance. The feedback signal captured by the IMU will be inputted to the LQR controller to move the robot forward (backward) to reach
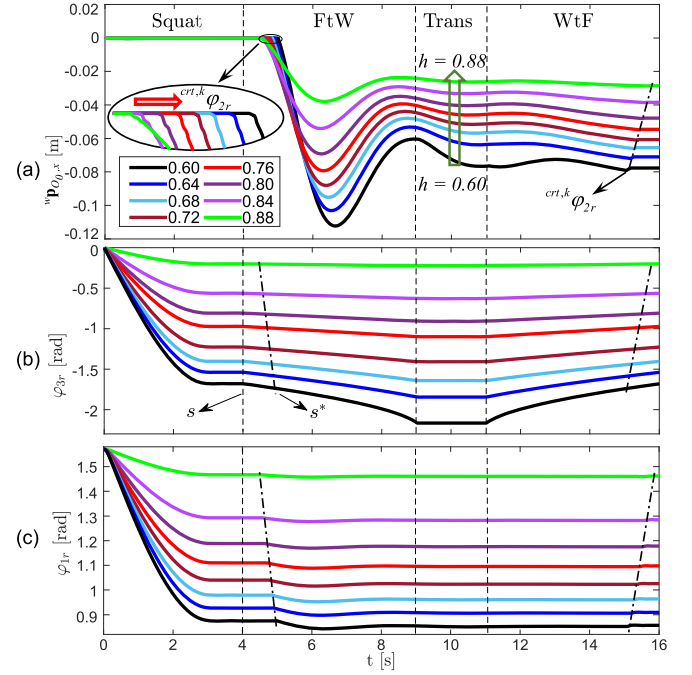

Fig. 9.   The simulation results of *in situ* FtW & WtF transformations for different h with the proposed algorithm. (a) The $^{w}\mathbf{p}_{O_0,x}$ during FtW and WtF transformations in different posture (different values of h with the unit of meter). The green arrow shows the increase direction of h from 0.60 m to 0.88 m. The inlet shows $^{crt}\varphi_{2_r}$ varies for different h, and the red arrow shows the increase direction of $^{crt}\varphi_{2_r}$. The dot-dashed line shows that the bigger $^{crt}\varphi_{2_r}$ is, the quicker the wheels leave the floor. (b) and (c) are the joint trajectories of φ_{1_r} and φ_{3_r} of these simulations, respectively. The dash line marked with **s** indicates the footed posture corresponding to different h. The dot-dashed line marked with **s*** indicates the corresponding critical postures.
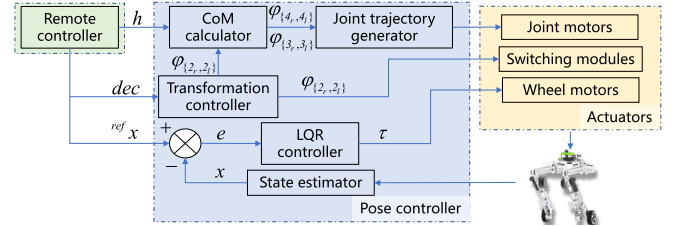

Fig. 10.   Overview of the control architecture. Symbols used in this diagram are introduced in Section II.

TABLE II
d_t OF TRANSFORMATIONS WITH & WITHOUT PROPOSED ALGORITHM

	Process	Max (m)	Min (m)	Average (m)	Std (m)
With	FtW	0.182	0.056	0.119	0.041
	WtF	0.011	0.004	0.006	0.002
Without	FtW	0.485	0.230	0.358	0.083
	WtF	0.342	0.174	0.258	0.054

the equilibrium state. On the contrary, despite different configurations, the displacement can be minimized by the proposed algorithm, as shown by the dashed lines. A comparison of trajectory length d_t is listed in Table II, which includes the maximum, the minimum, average and standard deviation of d_t in all trials. The d_t has been reduced by 67% (FtW) and 98% (WtF) in average in different configurations. This indicates the
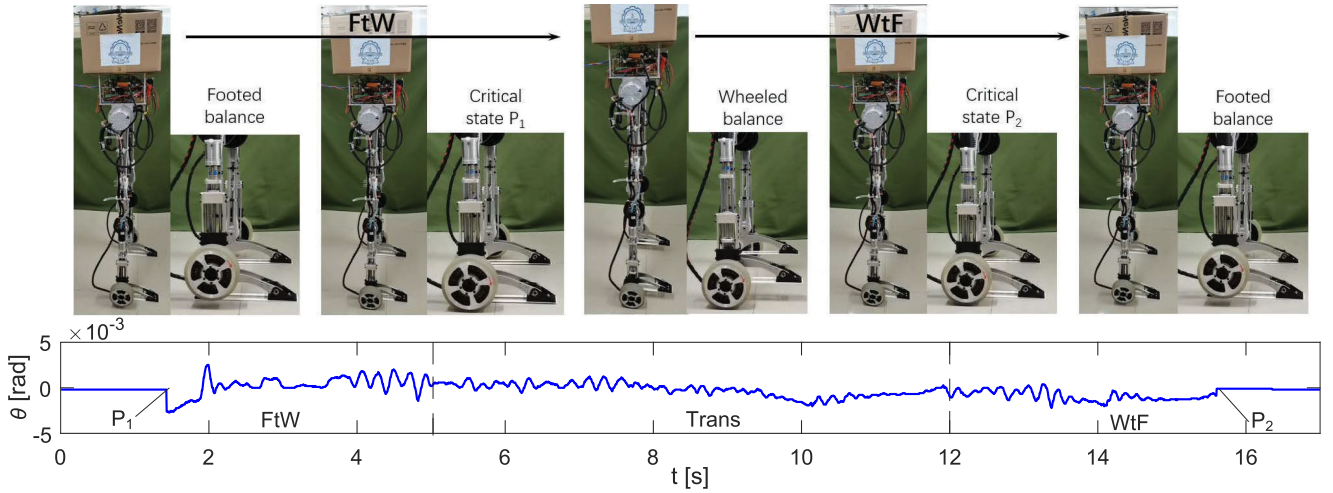
Fig. 11.   FtW and WtF transformations in the upright posture. Above the θ date diagram, the four plots shows the corresponding process of this experiment. The partial enlarged views are used to show the contact of wheels and feet with the ground more clearly. P_1 and P_2 in the θ diagram are critical positions and correspond to the second and fourth plots of the above process.
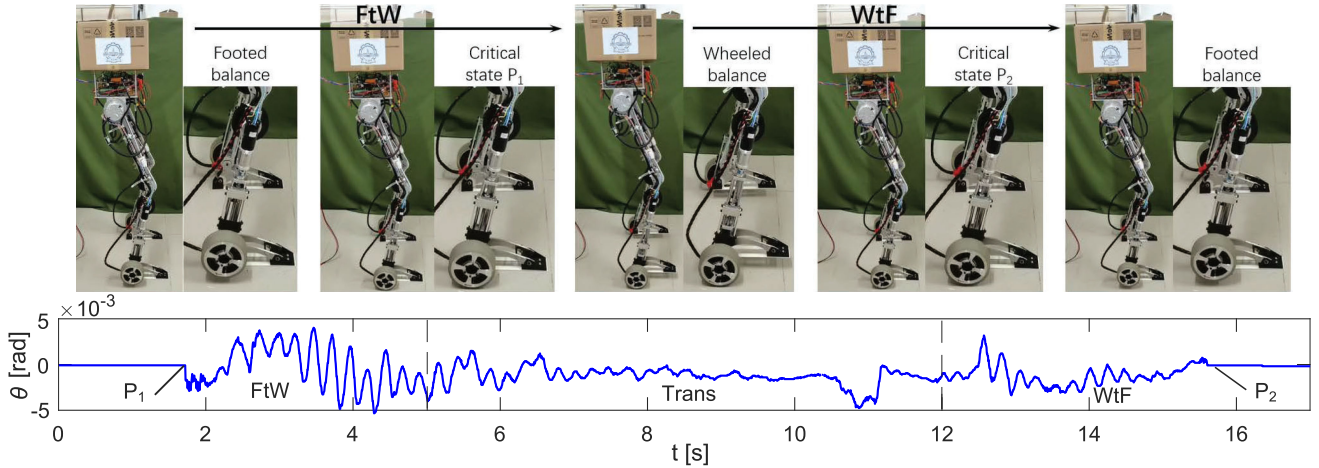

Fig. 12.   FtW and WtF transformations in a random posture.

projection-based algorithm is valid for achieving the aimed *in situ* transformation.

In addition, some characteristics of *in situ* transformation can be seen from Fig. 9. For both FtW and WtF, the greater h is, the smaller change of $^w\mathbf{p}_{O_0,x}$ will become. When the robot performs FtW, a smaller h corresponds to a smaller φ_{1_r}, which results in a greater forward sudden disturbance on the wheel when robot reaches the critical state. To compensate this disturbance, LQR controller will generate greater torque τ_{1_r}, τ_{1_l}. In contrast, when the robot performs WtF, before it reaches the critical state, the robot can achieve a smoother *in situ* transformation by adjusting its upper body simultaneously without a sudden disturbance. Fig. 9(b) and (c) show the joint trajectories of φ_{1_r} and φ_{3_r} of these simulations, respectively. Similar to $^w\mathbf{p}_{O_0,x}$, the smaller h is, the greater adjustments of φ_{1_r} and φ_{3_r} will be. With the proposed algorithm, the worst case of $^w\mathbf{p}_{O_0,x}$ during *in situ* transformation is 0.112 m. The adjustment amplitudes of φ_{1_r} and φ_{3_r} from current posture $\mathbf{s}$ to the targeted $\mathbf{s}^*$ are smaller than 0.1rd as shown in Fig. 9.

B. Experiments

1) Experimental Setup: The *SR600-II* system consists of two legs ending with actuated wheels and feet in parallel, as shown in Fig. 1. Each leg can be extended and retracted independently by actuating the corresponding motors installed in the hip and kneel joints. The foot and wheel are connected in parallel to the calf of each leg. This structure allows the robot conduct FtW and WtF transformations, as shown in Fig. 1(b). The velocities on both wheels can be estimated independently by incremental encoders installed on them. Table I lists the masses and lengths of *SR600-II*. In order to realize the simultaneous operation of multiple tasks, a control system was built based on μC/OS-III. As shown in Fig. 10, the architecture consists of three parts including remote controller, pose controller and actuators. The desired actions can be manually inputted by user from the remote controller to adjust the robot height h, perform transformation under a decision *dec*, and define a target state ^{ref}x for *SR600-II* to track.

2) in Situ Transformation: In this part, we carried out experiments on the *SR600-II* both in a upright and a random postures.

In these experiments, the robot performed FtW in 1∼5 s. And there was a transient period (5∼12 s) before performing WtF in 12∼17 s. The experimental scenes and data of these two experiments are shown in Fig. 11 and Fig. 12. In these figures, P_1 and P_2 correspond to the moment that the robot reaches the critical states for FtW and WtF, respectively. Compared with the upright posture shown in Fig. 11, the squat posture shown in Fig. 12 took more time to reach the critical state of FtW (P_1). The former one finished at 1.42 s and the latter one finished at 1.71 s. On the contrary, the former one reached P_2 at 15.58 s and the latter one reached at 15.29 s. This was because the critical value $^{crt}\varphi_{2_r}$ of the squat posture was greater than the one of upright posture. The d_t in the squat posture was also slightly greater than the one performed in the upright posture. The tilt angles (θ) were more volatile because there was more disturbance in the system, which was also more challenging to the hardware and controller.

V. CONCLUSION

This paper proposed an *in situ* transformation method for wheel-biped robot. The kinematic and LIP-based dynamic models have been presented to facilitate the control of the *in situ* transformation. Through the workspace analyses we showed that FtW transformation was a more stringent process than the WtF one. Then the control strategy of *in situ* wheel-biped transformation was proposed based on the relationship between footed workspace and the critical one. Finally, the feasibility of modeling and control strategy have been demonstrated by various simulations and experiments on the current prototype. In the future, vision-based intelligent system will be studied to make the robot automatically decide when to perform the wheel-biped transformation.

REFERENCES

[1] M. Hutter *et al.*, "Anymal-a highly mobile and dynamic quadrupedal robot," in *Proc. IEEE/RSJ Int. Conf. Intell. Robots Syst.*, 2016, pp. 38–44.
[2] Spot. [Online]. Available: https://robots.ieee.org/robots/spotmini/
[3] Boston Dynamics' Marc Raibert on Next-Gen ATLAS, "A Huge Amount of Work," [Online]. Available: https://spectrum.ieee.org/automaton/robotics/humanoids/boston-dynamics-marc-raibert-on-nextgen-atlas
[4] Agility Robotics. Building Robots to Work in Human Spaces: 2020 ICRA Presentation. Youtube. [Online]. Available: https://youtu.be/SxSJjfNvHWc
[5] E. Ackerman, "Honda robotics unveils next-generation ASIMO robot," [Online]. Available: https://spectrum.ieee.org/automaton/robotics/humanoids/honda-robotics-unveils-next-generation-asimo-robot
[6] W. Roozing, Z. Ren, and N. G. Tsagarakis, "An efficient leg with series-parallel and biarticular compliant actuation: Design optimization, modeling, and control of the eleg," *Int. J. Robot. Res.*, vol. 40, no. 1, pp. 37–54, 2021.
[7] S. Jeong and T. Takahashi, "Wheeled inverted pendulum type assistant robot: Design concept and mobile control," *Intell. Serv. Robot.*, vol. 1, no. 4, pp. 313–320, 2008.
[8] S. R. Kuindersma, E. Hannigan, D. Ruiken, and R. A. Grupen, "Dexterous mobility with the uBot-5 mobile manipulator," in *Proc. Int. Conf. Adv. Robot.*, 2009, pp. 1–7.
[9] M. Stilman, J. Olson, and W. Gloss, "Golem krang: Dynamically stable humanoid robot for mobile manipulation," in *Proc. IEEE Int. Conf. Robot. Automat.*, 2010, pp. 3304–3309.
[10] C. H. G. Li, L. P. Zhou, and Y. H. Chao, "Self-balancing two-wheeled robot featuring intelligent end-to-end deep visual-steering," *IEEE/ASME Trans. Mechatronics*, vol. 26, no. 5, pp. 2263–2273, Oct. 2021.
[11] T. Klamt and S. Behnke, "Anytime hybrid driving-stepping locomotion planning," in *Proc. IEEE/RSJ Int. Conf. Intell. Robots Syst.*, 2017, pp. 4444–4451.
[12] M. Bjelonic *et al.*, "Keep rollin'–whole-body motion control and planning for wheeled quadrupedal robots," *IEEE Robot. Automat. Lett.*, vol. 4, no. 2, pp. 2116–2123, Apr. 2019.
[13] N. Kashiri *et al.*, "CENTAURO: A hybrid locomotion and high power resilient manipulation platform," *IEEE Robot. Automat. Lett.*, vol. 4, no. 2, pp. 1595–1602, Apr. 2019.
[14] H. Peng, J. Wang, S. Wang, W. Shen, D. Shi, and D. Liu, "Coordinated motion control for a wheel-leg robot with speed consensus strategy," *IEEE/ASME Trans. Mechatronics*, vol. 25, no. 3, pp. 1366–1376, Jun. 2020.
[15] A. Bouton, C. Grand, and F. Benamar, "Design and control of a compliant wheel-on-leg rover which conforms to uneven terrain," *IEEE/ASME Trans. Mechatronics*, vol. 25, no. 5, pp. 2354–2363, Oct. 2020.
[16] J. Chen, K. Xu, and X. Ding, "Roller-skating of mammalian quadrupedal robot with passive wheels inspired by human," *IEEE/ASME Trans. Mechatronics*, vol. 26, no. 3, pp. 1624–1634, Jun. 2021.
[17] Boston Dynamics. Handle. [Online]. Available: https://robots.ieee.org/robots/handle
[18] V. Klemm *et al.*, "LQR-assisted whole-body control of a wheeled bipedal robot with kinematic loops," *IEEE Robot. Automat. Lett.*, vol. 5, no. 2, pp. 3745–3752, Apr. 2020.
[19] X. Li, H. Zhou, H. Feng, S. Zhang, and Y. Fu, "Design and experiments of a novel hydraulic wheel-legged robot (WLR)," in *Proc. IEEE/RSJ Int. Conf. Intell. Robots Syst.*, 2018, pp. 3292–3297.
[20] H. Chen, B. Wang, Z. Hong, C. Shen, P. M. Wensing, and W. Zhang, "Underactuated motion planning and control for jumping with wheeled-bipedal robots," *IEEE Robot. Automat. Lett.*, vol. 6, no. 2, pp. 747–754, Apr. 2021.
[21] K. Hashimoto *et al.*, "Realization by biped leg-wheeled robot of biped walking and wheel-driven locomotion," in *Proc. IEEE Int. Conf. Robot. Automat.*, 2005, pp. 2970–2975.
[22] J. Lim *et al.*, "Robot system of DRC-HUBO and control strategy of team KAIST in darpa robotics challenge finals," *J. Field Robot.*, vol. 34, no. 4, pp. 802–829, 2017.
[23] T. Liu, C. Zhang, S. Song, and M. Q.-H. Meng, "Dynamic height balance control for bipedal wheeled robot based on ROS-Gazebo," in *Proc. IEEE Int. Conf. Robot. Biomimetics*, 2019, pp. 1875–1880.
[24] C. Zhang, T. Liu, S. Song, and M. Q.-H. Meng, "System design and balance control of a bipedal leg-wheeled robot," in *Proc. IEEE Int. Conf. Robot. Biomimetics*, 2019, pp. 1869–1874.
[25] C. Zhang, T. Liu, S. Song, J. Wang, and M. Q.-H. Meng, "Dynamic wheeled motion control of wheel-biped transformable robots," *Biomimetic Intell. Robot.*, 2021, Art. no. 100027, doi: 10.1016/j.birob.2021.100027.
[26] M. Vukobratović and B. Borovac, "Zero-moment point–thirty five years of its life," *Int. J. Humanoid Robot.*, vol. 1, no. 01, pp. 157–173, 2004.
[27] A. Tözeren, *Human Body Dynamics: Classical Mechanics and Human Movement*. New York, NY, USA: Springer, 1999.